

Contents lists available at ScienceDirect

Journal of Crystal Growth

journal homepage: www.elsevier.com/locate/jcrysgro





Analysis of interface roughness in strained InGaAs/AlInAs quantum cascade laser structures ($\lambda \sim 4.6~\mu m$) by atom probe tomography

B. Knipfer ^{a,*}, S. Xu ^b, J.D. Kirch ^a, D. Botez ^a, L.J. Mawst ^a

- a Department of Electrical and Computer Engineering. University of Wisconsin-Madison. 1415 Engineering Drive. Madison. WI 53706. USA
- b Department of Material Science and Engineering, University of Wisconsin-Madison, 1415 Engineering Drive, Madison, WI 53706, USA

ARTICLE INFO

Communicated by Robert Feigelson

Keywords:

- A1. Atom probe tomography
- A1. Interfaces
- A3. Organometallic vapor phase epitaxy
- A3. Superlattices
- B2. Semiconducting III-V materials
- B3. Quantum cascade lasers

ABSTRACT

In this study, in-plane interface roughness (IFR) values are extracted via atomic probe tomography (APT) for a few key interfaces within a quantum cascade laser (QCL) active region composed of compressively-strained InGaAs quantum wells (QWs) and tensilely-strained AlInAs barriers. The structure was grown by organometallic vapor phase epitaxy (OMVPE) at 605 °C, 100 rpm, 100 torr, with a 5 s interruption time between layers. The full-stage thickness measured via high-resolution x-ray diffraction (HR-XRD) is used to calibrate the reconstruction to within 5%. From the APT results, it is found that interfaces to two barriers of different tensile-strain value (i.e., of different Al concentration) have different RMS-roughness amplitude. Specifically, barriers of higher Al concentration have ~50% larger RMS-roughness amplitude, as the strain differential increases by a factor of 2.2. To the best of our knowledge, this is the first experimental data showing that roughness parameters within a QCL active region are different interfaces within the same grown structure.

1. Introduction

Since the first experimentally demonstrated quantum cascade laser (QCL) in 1994 at Bell Labs, achieving high output power, low threshold-current density, and reduced temperature sensitivity of the devices electro-optical characteristics have been active areas of research. Many QCLs that are grown via molecular beam epitaxy (MBE), as well as fabricated in industry, generally employ a conventional structure having constant composition alloys, while varying the well and barrier widths. However, it has been shown that for state-of-the-art devices targeting high power and, more importantly, strong carrier-leakage suppression for high efficiency, deviation from the conventional structure to a steptapered active-region (STA) structure is necessary [1].

Until recently, the carrier-leakage process in QCL structures was modeled assuming longitudinal-optical (LO)-phonon scattering as the only scattering mechanism between energy states. However, recent studies have shown that the addition of interface roughness (IFR) scattering as another carrier-leakage trigger is essential to bridging the gap between theoretical and experimental internal efficiency values [2]. As QCLs are becoming more commercially available and volume manufacturing is emerging, the need for accurate modeling and device-performance projections is essential for device design and material

growth.

Characterizing the IFR parameters of the interfaces between the layers comprising the QCL-superlattice (SL) active region is necessary to further optimize device performance and potentially achieve higher wall-plug efficiencies. Previous work has focused on interface grading via transmission electron microscopy (TEM) [3] and extracting the IFR parameters from device performance of MBE- grown [2,4-7] and OMVPE-grown QCLs [2,8]. Here we use APT to directly characterize the interface roughness for specific interfaces of varying Al concentration within a single QCL- structure growth performed via OMVPE. Previously APT has been used to investigate the amount of intermixing [9], the effect of thin layers on Al incorporation [10], and indium segregation at interfaces [11]. The method of extracting in-plane IFR parameters utilized here is described by Grange et al. [12] and Mukherjee et al. [13], however, instead of investigating Si to SiGe interfaces for THz devices grown via ultrahigh-vacuum chemical vapor deposition (UHV-CVD), we are investigating interfaces between InGaAs and AlInAs layers for mid-IR-emitting devices grown via OMVPE.

A typical QCL structure has 30 to 50 stages; each stage containing \sim 20 interfaces. These interfaces play a direct role in carrier lifetimes and carrier transport. The scattering rate due to IFR is proportional to the conduction band (CB) offset squared and the overlap of the

E-mail address: bknipfer@wisc.edu (B. Knipfer).

^{*} Corresponding author.

wavefunctions at the interface [1]. The largest CB offsets occur on the downstream side of the active region as well as in the extractor region, leading to IFR scattering dominating the lower-laser level lifetime as well as the shunt-type carrier leakage triggered from the upper-laser level and injector-region states [2]. Thus, IFR scattering is a critical parameter which directly impacts the threshold-current density and internal efficiency.

Individual interfaces were probed using isoconcentration surfaces between the peak InGaAs-layer composition and peak AlInAs-layer composition to best represent the center of the compositionally graded region. This was done for layers of different aluminum and gallium concentrations across multiple stages. Using a height-height correlation function (HHCF) we were able to extract the roughness amplitudes (Δ) and in-plane correlation lengths (Λ). We find a large difference in the roughness amplitude between InGaAs/AlInAs interfaces of different Al concentrations and, in turn, different strain differentials.

The current models for IFR scattering use two parameters for the entire QCL structure, assuming constant roughness. However, highpower QCL designs employ a step-tapered active region (STA) or a linear-tapered active region with varying layer compositions [1,14,15]. Employing APT, we have analyzed the IFR of strained InGaAs/AlInAs STA-type QCLs grown by OMVPE and show that the roughness of interfaces vary for different layer compositions in a full QCL structure, thus more complex models are required to properly account for the impact of IFR scattering on state lifetimes and carrier leakage.

2. Materials and methods

A full QCL structure emitting at $\lambda \sim 4.55~\mu m$ was grown on a (001) InP substrate by OMVPE in a close-coupled showerhead (3 \times 2") configuration at a temperature of 605 °C. The reactor pressure was held at 100 torr, a 5 sec interruption time was used between layers, and the susceptor was rotated at 100 rpm. The target compositions, V/III ratios, group-III partial pressures, and growth rates are shown in Table 1.

Growth sources included: trimethylindium (TMIn), trimethylgallium (TMGa), trimethylaluminum (TMAl), phosphine, and arsine. An Epison was employed in a feedback loop to control the TMIn concentration.

The structure analyzed is a 40-stage QCL. The active region consists of the following: (14), 30, [14], 34, 11, [42], 11, [11], 34, (19), 23, 20, $\underline{21}, \underline{24}, \underline{19}, \underline{22}, 14$, [20], 14, (21), [13], and [(22)], where the bold script is $In_{0.65}Ga_{0.35}As$, underlined is doped, italicized is $In_{0.75}Ga_{0.25}As$, italicized in parenthesis is $In_{0.2}Al_{0.8}As$, bracketed script is AlAs, bracket bolded is $In_{0.69}Ga_{0.31}As$, bracket italic is $In_{0.65}Ga_{0.35}As$, parenthesis bold is $In_{0.69}Ga_{0.31}As$, bracket italic is $In_{0.65}Ga_{0.35}As$, parenthesis bold italic is $In_{0.76}Ga_{0.34}As$, italic bold is $In_{0.3}Al_{0.7}As$, parenthesis bold italic is $In_{0.76}Ga_{0.3}As$, bracket bold italic is $In_{0.25}A-l_{0.75}As$, and bracket and parenthesis is $In_{0.76}Ga_{0.24}As$. Below the core region there is a 0.1 μ m-thick $In_{0.53}Ga_{0.47}As$ layer lattice-matched to InP and doped at $n=5\times10^{16}~{\rm cm}^{-3}$ that acts as the lower part of waveguide to increase the optical-mode confinement factor, followed by a lower cladding layer consisting of a 2 μ m-thick, doped at $n=2\times10^{16}~{\rm cm}^{-3}$, InP. Directly above the core region there is another 0.1 μ m-thick $In_{0.53}Ga_{0.47}As$ layer, doped at $n=5\times10^{16}~{\rm cm}^{-3}$, as the upper part of the

Table 1V/III ratios and growth rates for layers grown within the active region.

Layer	Target Composition	V/III Ratio	Group III Partial Pressure (Torr)	Growth Rate (nm/s)
2nd Well 3rd Well 1st & 2nd Active- Region Barrier	$\begin{array}{c} In_{0.69}Ga_{0.31}As \\ In_{0.75}Ga_{0.25}As \\ Al_{0.65}In_{0.35}As \end{array}$	321.4 256.4 499.3	1.55E-3 1.94E-3 9.96E-4	0.120 0.151 0.081
3rd Active- Region Barrier	AlAs	741.1	6.71E-4	0.059

waveguide, a 3 µm-thick InP upper cladding layer, doped at $n=2\times 10^{16}~cm^{-3}$, and finally a 1 µm-thick highly-doped InP (2 \times 10 $^{19}~cm^{-3}$) layer that acts as the contact layer. The full structure was calibrated postgrowth with high-resolution x-ray diffraction (HR-XRD).

A ${\rm Ga}^+$ -focused ion beam (Ga-FIB) was employed to create lift-out samples to prepare APT tips. A thin (~ 500 nm) Pt layer was used as a protective cap layer for the lift-out preparation and tip shaping. The tips were welded onto a Si micro-post array using Pt. The APT tips were shaped with an accelerating voltage of 30 kV and progressively lower beam currents. After shaping, a final cleaning step was performed at an accelerating voltage of 2 kV and a beam current of 100 pA to remove ${\rm Ga}^+$ that implanted during the tip shaping.

The atom probe data was collected with a LEAP5000XS in the pulsed-laser mode at a sample temperature of 30 K to maximize the spatial resolution with a pulse frequency of 500 kHz and an energy of 1.0 pJ. This instrumentation is capable of reaching a collection efficiency of nearly 80% allowing the investigation of extremely thin layers and interfaces.

Reconstruction was performed using the shank angle method in order to account for the changing evaporation field between alternating layers of AlInAs and InGaAs. The reconstruction was calibrated such that the full stage thickness is within 5% of the measured value from HRXRD, as shown in Fig. 1, which correlates with a potential 5% error within each interface. The voxel size is 2 nm by 2 nm in the in-plane direction and 0.5 nm in the growth direction. A small voxel size increases resolution at the expense of potential statistical error and the inverse is true as well. Three interfaces of interest were analyzed across three stages of the full reconstruction. These interfaces are identified in Fig. 2. Also shown in Fig. 2, are the calculated fractions of leakage-current densities relative to the threshold-current density at each interface, which are influenced by the IFR scattering occurring at a particular interface [2].

In Fig. 2, the growth direction is from right to left. The first interface is $In_{0.69}Ga_{0.31}As \rightarrow Al_{0.65}In_{0.35}As$ and the second interface is in inverse order: $Al_{0.65}In_{0.35}As \rightarrow In_{0.69}Ga_{0.31}As$. These two interfaces were chosen to be analyzed as they are the thinnest layers in the structure (1.1 nm), have the same compositional target, and bound the same InGaAs well, allowing us to observe any difference in roughness parameters when entering or exiting an AlInAs barrier which has previously been shown to have an asymmetry for MBE-grown devices [5]. The third interface analyzed is AlAs $\rightarrow In_{0.75}Ga_{0.25}As$ since it has the highest Al concentration, and thus the highest strain. This interface typically plays the largest role in active-region carrier leakage because it has overlap with the energy state above the upper-laser level and the largest conduction band offset.

Isoconcentration surfaces were defined at each identified interface as outlined by Grange et al. [12], however, we are analyzing a more complex system which includes ternaries and quaternaries [9,10]. As such, we define the interface as the point at which the Al concentration is half the value between the maximum value in the AlInAs barrier and the minimum value in the adjacent InGaAs well. The isoconcentration surfaces can then be investigated using a height-height correlation function (HHCF) as shown in Equation (1).

$$H(\overrightarrow{\tau}) = \langle |h(\overrightarrow{\rho}) - h(\overrightarrow{\rho} + \overrightarrow{\tau})|^2 \rangle_{\overrightarrow{\rho}} \tag{1}$$

 $h(\overrightarrow{\rho})$ is the height of the isoconcentration surface relative to the mean plane as a function of position and $\overrightarrow{\tau}$ is a vector such that the dependence of the difference in height squared can be plotted as a function of position throughout the isoconcentration surface.

3. Results

Using the methods outlined above, we generated HHCF graphs for the various interfaces across three stages. Examples of these graphs are shown in Figs. 3 and 4. At small $\vec{\tau}$ values there is a strong dependence

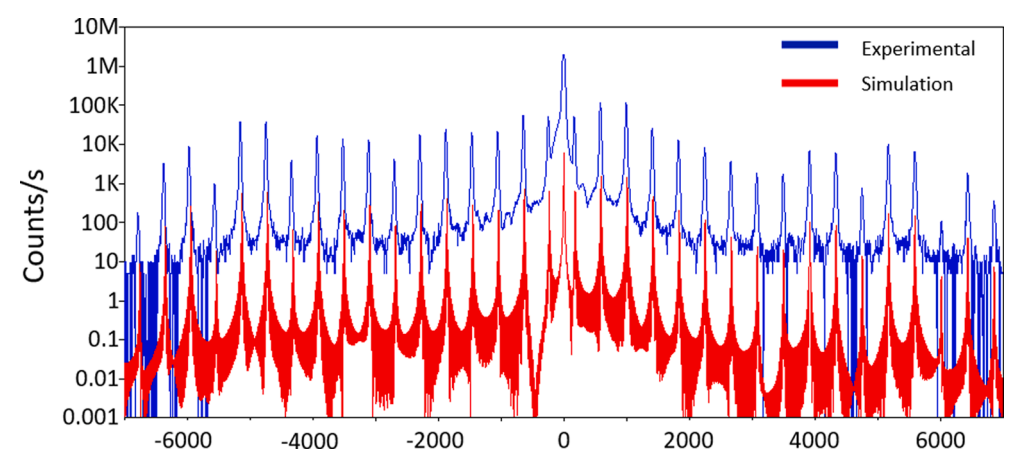


Fig. 1. Experimental HR-XRD is shown in blue, and the simulation is shown in red. Using the simulation, the thicknesses and compositions of the final structure can be extracted by matching the simulated to experimental spectra.

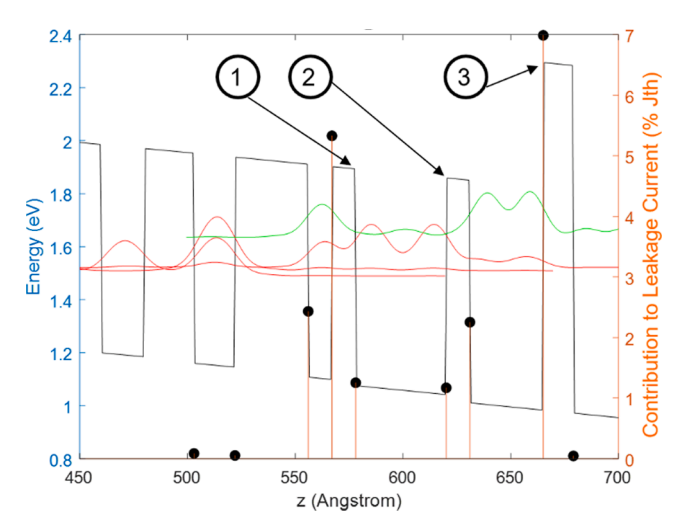


Fig. 2. Conduction band diagram of the active region corresponding to the left y-axis, the percent of threshold-current density that is lost at each interface corresponds to the black dots and the right y-axis for the analyzed structure. The red curves represent ground states and the upper lasing level wavefunctions while the green curve is the wavefunction above the upper laser level (ul + 1). The growth direction is from right to left.

on position, however, as $\overrightarrow{\tau}$ increases it becomes less dependent. Ideally, at large $\overrightarrow{\tau}$ values this dependency is lost. However, we have seen that at larger $\overrightarrow{\tau}$ values there can be oscillations, as shown in Fig. 3. These oscillations may be an artifact reflecting some degree of non-planarity in the APT reconstruction over the entire iso-concentration surface and can also be found in previous work extracting these parameters [12,13]. To avoid the impact on the fit, we focus on fitting the knee of the HHCF where the two relevant IFR parameters are located.

Using Equation (2), we can extract the relevant in-plane IFR parameters, Δ and Λ , which correspond to the RMS roughness and in-plane correlation length, respectively, by fitting the HHCF.

$$H(\overrightarrow{\tau}) = 2\Delta^2 \left[1 - exp\left(-\left(\frac{\overrightarrow{\tau}^2}{\Lambda}\right) \right) \right]$$
 (2)

This calculation was performed for the three identified interfaces through three stages of the evaporated structure. The average values and their standard deviations are shown in Table 2.

The interfacial mixing width was also investigated, as this was also previously analyzed by Rajeev et al. [9] for the same material system. The mixing width here was extracted by fitting the 1-D concentration

profile with the function in Equation (3), where c_0 and d_0 are the offset and scaling parameters, respectively, z_0 is the position offset, and L is defined as the distance over which the composition changes from 12% to 88% of the peak and minimum values [12].

$$c(z) = c_0 + d_0 erf \left[\frac{2\sqrt{\ln(2)} (z - z_0)}{L} \right]$$
 (3)

The extracted interfacial mixing widths are compiled in Table 2. The average interdiffusion length found previously [9] was 0.55 nm, which, although was extracted assuming diffusion-driven intermixing, is characterizing a similar property. This is well in-line with the extracted interfacial mixing widths extracted here. Our extracted values are half the value extracted by Grange et al. [12] for Si/SiGe THz QCLs grown via UHV-CVD. The stages analyzed here were consecutive within the growth. As we do not have the upper or lower confinement layers we cannot tell where within the 40 stages these are located. Previously we looked at 12 stages within a growth and based off of the diffusion constant extracted by Rajeev [9] we would expect the change in interfacial mixing width to be quite small, and we did not see any change across 12 stages [10]. Ideally, all 40 stages are identical, practically there are likely some differences between the first and last stage.

The strain by layer relative to InP, shown in Table 2, is calculated using Equation (4) below.

$$\frac{a_{lnP} - a_{ln_sGa_{1-s}As}}{a_{lnP}} = Strain Relative to InP$$
 (4)

 a_{InP} is the lattice constant for InP, a_{InGaAs} is the lattice constant for In $_x$ Ga $_{1-x}$ As, and the same calculation can be performed for Al $_{1-x}$ In $_x$ As by replacing the In $_x$ Ga $_{1-x}$ As lattice constant with that of the Al $_{1-x}$ In $_x$ As. The differential strain relative to InP is calculated by taking the magnitude of the difference in strain at each interface.

From Table 2, we can see that the first two interfaces have very similar Δ and Λ values, showing that entering versus exiting a barrier or well for layers that share the same level of strain appears to not play a significant role in interface roughness. Bouzi et al. [5] have previously reported on 7.2 μ m-emitting devices grown by MBE that there may be some degree of asymmetry; however, for the results shown here, the difference is within the error bars. It is possible that different interfaces within the structure have higher asymmetry; extracting the remainder of the interface parameters is ongoing and will lead to a better understanding of all the interfaces. The interfaces here were chosen as they included the barrier with the highest aluminum target concentration, barriers with lower aluminum targets, and allowed the comparison of an upstream vs downstream interface. Comparing the AlAs \rightarrow In_{0.75}Ga_{0.25}As interface with the other two interfaces we can see a large discrepancy in the extracted Δ values. We see roughly a 50% increase in

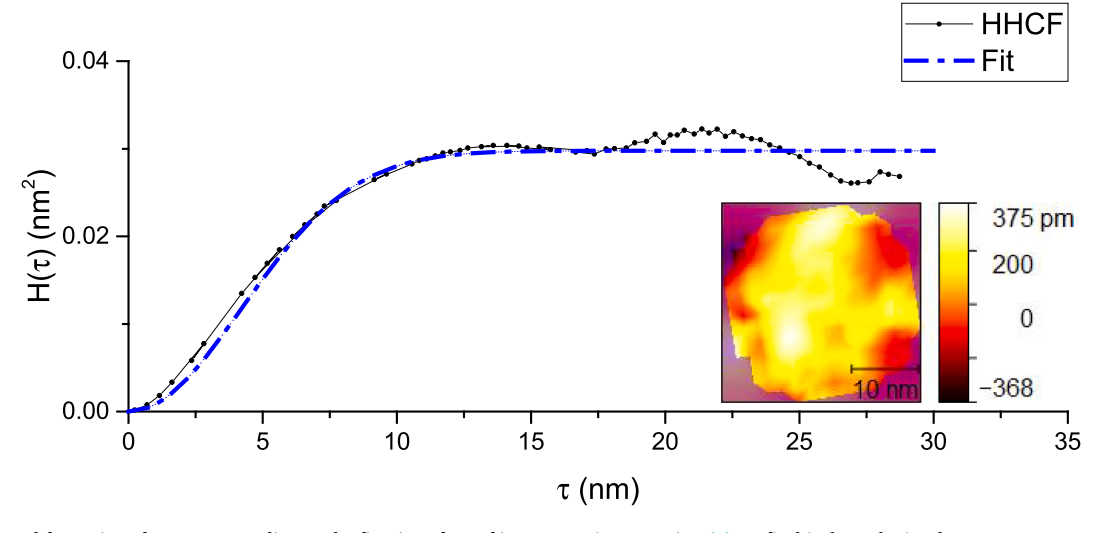


Fig. 3. HHCF plotted for an interface corresponding to the first interface of interest. Using Equation (2), to fit this data, the in-plane IFR parameters are extracted to be $\Delta=0.122$ nm and $\Lambda=5.94$ nm. The isoconcentration surface analyzed is inset.

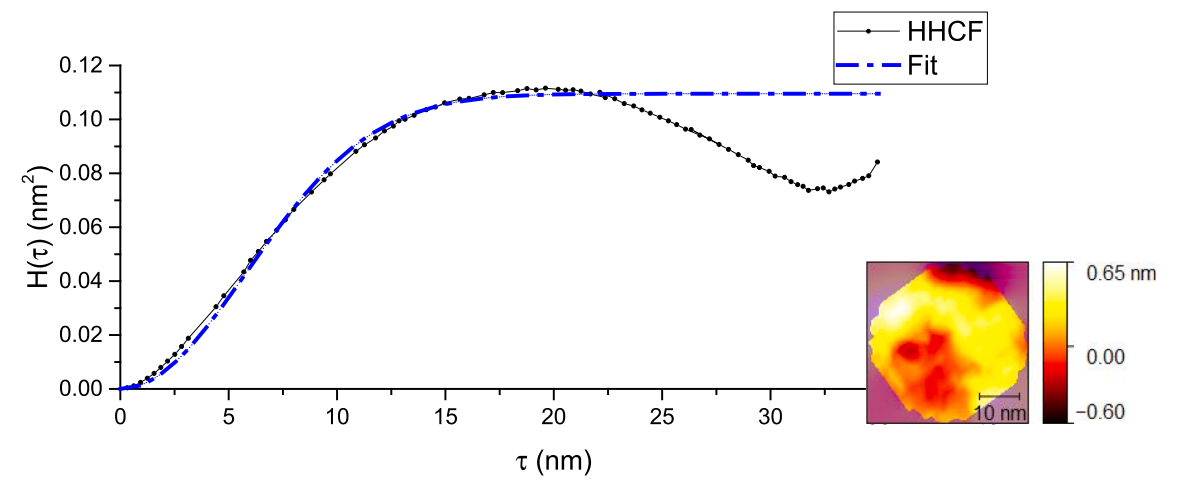


Fig. 4. HHCF plotted for an interface of the 3rd active-region barrier which has the highest aluminum concentration target, AlAs. The extracted in-plane IFR parameters are $\Delta=0.234$ nm and $\Lambda=8.21$ nm. The isoconcentration surface analyzed is inset.

Table 2

Extracted IFR parameters and interfacial mixing width from the three interfaces of interest averaged across 3 stages. The column labeled differential strain relative to InP is the magnitude of the strain between the compressive-strained barrier and tensile-strained well. The contribution from each layer is shown in the column labeled as strain by layer where negative values correspond to layers compressive-strained and positive for tensile-strained.

Interface	Δ (nm)	Λ (nm)	Interfacial Mixing Width (nm)	Strain by Layer Relative to InP (%)	Differential Strain Relative to InP (%)
$In_{0.69}Ga_{0.31}As \rightarrow Al_{0.65}In_{0.35}As$	$0.145~(\pm~0.02)$	6.61 (\pm 0.76)	0.54 (± 0.05)	-0.011 → 0.012	2.3
$Al_{0.65}In_{0.35}As \to In_{0.69}Ga_{0.31}As$	$0.120~(\pm~0.01)$	$5.75~(\pm~0.36)$	$0.61~(\pm~0.08)$	$0.012 \rightarrow -0.011$	2.3
AlAs \rightarrow In _{0.75} Ga _{0.25} As	$0.201~(\pm~0.02)$	$7.08~(\pm~1.06)$	$0.68~(\pm~0.2)$	$0.035 \rightarrow -0.015$	5.0

the RMS roughness amplitude, Δ . We can also see that the differential strain, defined to be the sum of the strain between the two layers of interest relative to InP, increases by a factor of about 2.2, thus showing a potential correlation with the increase in the Δ value squared. This could additionally be the result of higher oxygen incorporation in the higher aluminum containing layers. These values are similar in magnitude to values previously extracted [4,6–8].

$$\frac{1}{\tau_{ii}^{IFR}} \ \Delta^2 \Lambda^2 \delta U^2 \tag{5}$$

The IFR scattering rate is proportional to Δ^2 , Λ^2 , and δU^2 as shown in

Equation (5) [1], where δU is the conduction band offset. A 50% increase in the Δ value, as measured here, would result in a scattering rate more than two times higher than the previous value for a particular interface. Variations in the roughness values for different interfaces will, in turn, have a significant impact on the IFR scattering rates and leakage currents for these devices. For an accurate model, one should consider varying roughness parameters for interfaces throughout a full QCL active-region structure.

4. Conclusion

We have shown that layers of different Al concentration and, in turn, different levels of differential strain result in significantly different RMS roughness values in InGaAs/AlInAs SL structures. However, we are unable to decouple the strain effects from effects originating from different Al contents. When comparing an interface of a barrier with a target composition of Al_{0.65}In_{0.35}As to that of a barrier with a target composition of AlAs, we see that the interface to the barrier with the higher Al concentration shows a nearly 50% greater RMS amplitude, which correlates with the change in differential strain at the respective interfaces. Characterizing the IFR parameters for all interfaces within the QCL structure will enable IFR engineering of the QCL structure for achieving further enhancements in device performance. In addition, OMVPEgrowth optimization can be carried out to reduce the roughnessparameters values for key interfaces within QCL structures. Future work will focus on extracting parameters from more interfaces and the integration of these variable parameters into a full scattering model.

CRediT authorship contribution statement

B. Knipfer: Investigation, Conceptualization, Methodology, Visualization, Software, Writing – original draft. **S. Xu:** Investigation. **J.D.** Kirch: Investigation. **D. Botez:** Conceptualization, Supervision, Writing – review & editing. **L.J. Mawst:** Conceptualization, Supervision, Writing – review & editing.

Declaration of Competing Interest

The authors declare that they have no known competing financial interests or personal relationships that could have appeared to influence the work reported in this paper.

Acknowledgement

This work is supported by AFOSR under Grant FA9550-19-1-0385,

NSF ECCS 1806285, and U.S. Army Research Office SBIR (Award No. W911NF-16-C-0116). Atom-probe tomography was performed at the Northwestern University Center for Atom-Probe Tomography (NUCAPT). The LEAP tomograph at NUCAPT was purchased and upgraded with grants from the NSF-MRI (DMR-0420532) and ONR-DURIP (N00014-0400798, N00014-0610539, N00014-0910781, N00014-1712870) programs. NUCAPT received support from the MRSEC program (NSF DMR-1720139) at the Materials Research Center, the SHyNE Resource (NSF ECCS-1542205), and the Initiative for Sustainability and Energy (ISEN) at Northwestern University. The authors gratefully acknowledge use of facilities and instrumentation at the UW-Madison Wisconsin Centers for Nanoscale Technology partially supported by the NSF through the University of Wisconsin Materials Research Science and Engineering Center (DMR-1720415).

References

- [1] D. Botez, et al., Opt. Mater. Express 8 (2018) 1378–1398, https://doi.org/10.1364/ OME.8.001378.
- [2] C. Boyle, et al., Appl. Phys. Lett. 117 (2020), 051101, https://doi.org/10.1063/ 5.0007812.
- [3] P. Offermans et al, Appl. Phys. Lett. Vol. 83, 4131 (2003) 10.1063/1.1627942.
- [4] A.Vasanelli et al, Appl. Phys. Lett. Vol. 89, 172120 (2006) 10.1063/1.2361264
- [5] P. Bouzi, et al., Appl. Phys. Lett. 116 (2014), 034504, https://doi.org/10.1063/ 1.4890311.
- [6] M. Franckie et al, Opt. Express, Vol. 23, 5201 (2015) 10.1364/OE.23.005201.
- [7] M. P. Semtsiv et al, Appl. Phys. Lett. Vol.113, 121110 (2018) 10.1063/1.5049090.
- [8] K. M. Oresick et al., AIP Advances, Vol.11, 025004 (2021) 10.1063/5.0037761.
- [9] A. Rajeev et al, Crystals, Vol. 8, 2018, 437 10.3390/cryst8110437.
- [10] B. Knipfer et al, Journal of Crystal Growth, Vol. 535, 2020, 125550. 10.1016/j. jcrysgro.2020.125550.
- [11] C.A. Wang, et al., J. Cryst. Growth 464 (2017) 215–220, https://doi.org/10.1016/j.jcrysgro.2016.11.029.
- [12] T. Grange et al, Phys. Rev. Applied, Vol. 13, 2020, 044062. 10.1103/ PhysRevApplied.13.044062.
- [13] S. Mukherjee, et al., ACS Appl. Mater. Interfaces 12 (2020) 1728–1736, https://doi.org/10.1021/acsami.9b13802.
- [14] D. Botez, et al., IEEE J. Sel. Top. Quantum Electron. 19 (2013) 1200312, https://doi.org/10.1109/JSTQE.2012.2237387.
- [15] D. Botez, C.-C. Chang, L.J. Mawst, J. Phys. D: Appl. Phys. 49 (2016), 043001, https://doi.org/10.1088/0022-3727/49/4/043001.